Research Square

Preprints are preliminary reports that have not undergone peer review.
They should not be considered conclusive, used to inform clinical practice,
or referenced by the media as validated information.

Physics-Informed Neural Modeling of TiO 2 Photoanode Thickness-Dependent Electron Transport and Photovoltaic Performance in Dye-Sensitized Solar Cells

K Sanyasi Naidu

s.kilaparthi@gmail.com

Jawaharlal Nehru Technological University, Kakinada

Nalluri Mohan Rao

Jawaharlal Nehru Technological University, Kakinada

Research Article

Keywords: Dye-Sensitized Solar Cell (DSSC), Tio2 Photoanode, Film Thickness, Physics-Informed Neural Network (PINN), Physics-Informed Extreme Learning Machine, Electron Diffusion, Recombination, Small-Data Modeling, Cross-Validation

Posted Date: September 14th, 2026

DOI: https://doi.org/10.21203/rs.3.rs-10792598/v1

License: This work is licensed under a Creative Commons Attribution 4.0 International License.
Read Full License

Additional Declarations: No competing interests reported.

Physics-Informed Neural Modeling of TiO_2 Photoanode Thickness-Dependent Electron Transport and Photovoltaic Performance in Dye-Sensitized Solar Cells

K Sanyasi Naidu, Nalluri Mohan Rao

Dept. Mechanical Engineering, Jawaharlal Nehru Technological University, Kakinada, AP, India

ABSTRACT:

The thickness of a photoanode in dye-sensitized solar cells (DSSCs) simultaneously influences the dye-accessible volume, optical path length, electron-transport distance and recombination. To estimate this competition, a physics-informed neural network was constructed based on the six compressed TiO_2 photoanodes used by Tsai et al. The spatial state is expressed as a random-feature (RF) neural field $u_\theta(x_i, d)$, with normalized depth, $x_i = x/d$, and film thickness, d. The field is bound by a steady-state diffusion-generation-recombination equation, and extraction and zero-flux boundary conditions. In the 6 devices dataset, the contact-gradient current was mapped with a low-capacity regularized thickness correction, using the PDE result as a fixed value (inverse parameters effective electron diffusion coefficient, electron lifetime, effective photon flux and photon flux). The analytic solution of contact current and relative least square (L_2) error of 0.997–1.001 and 0.08–0.68 % respectively confirmed the neural field. The last device model resulted in training Mean Absolute Percentage Errors (MAPEs) of 7.03% for J_{SC}, 1.00% for V_{OC}, 1.55% for FF, and 6.44% for algebraically consistent efficiency. The efficiency MAPE of leave-one-thickness-out validation outperformed the results of linear regression (27.76%), quadratic regression (26.08%), natural cubic spline interpolation (78.42%), Gaussian-process regression (19.34%), and a conventional ANN (20.15%). The continuous model gave optimum thickness as 29.72 μm at 8.70% efficiency, while jackknife resampling revealed that the thickness has a significant uncertainty, as only six devices exist. A frozen model transfer to an independent published thickness series yielded the MAPE of 17.10%, indicating a low level of cross-system transfer, and a need for morphology and electrolyte-aware inputs. The study thus presents a physics-regularized small data framework that discriminates between within-system predictive value and universal DSSC generalization, which can be replicated.

Keywords: Dye-Sensitized Solar Cell (DSSC); Tio_2 Photoanode; Film Thickness; Physics-Informed Neural Network (PINN); Physics-Informed Extreme Learning Machine; Electron Diffusion; Recombination; Small-Data Modeling; Cross-Validation

Corresponding Author: K Sanyasi Naidu,
Mail ID: s.kilaparthi@gmail.com
Dept. Mechanical Engineering, Jawaharlal Nehru Technological University, Kakinada, AP, India

NOTATIONS

The principal symbols used in Sections 3-5 are listed below in the order of their first appearance and some of these symbols are provided with subscripts and superscripts as the equations call for. (1)-(7).

Symbol	Parameter (Name / Definition)	Units
X	Spatial coordinate (depth into the TiO_2 layer)	m
D	Photoanode (film) thickness	m (reported in μm)
ξ	Normalized depth coordinate, $\xi = x/d$	dimensionless, $0 \le \xi \le 1$
Z	Normalized thickness, $z = 2(d-d_{min})/(d_{max}-d_{min})-1$	dimensionless, $-1 \le z \le 1$
N_e	Illuminated (excess) electron density	m^{-3}
n_e^0	Dark reference electron density	m^{-3}

D_e	Effective electron diffusion coefficient	m^2/ s
τ	Electron lifetime	s
Φ	Effective photon flux	photons per (m^2 s)
α	Effective absorption coefficient	m^{-1}
L	Electron diffusion length, $L = \sqrt{(D_e\tau)}$	m (but μm in text)
u	Dimensionless excess electron density, $u = (n_e - n_e^0)/(\Phi\alpha\tau)$	Dimensionless
u_θ	Neural-field approximation of u (θ = trainable coefficients)	Dimensionless
q	Elementary charge	C
J_{PDE}	PDE-derived (nominal) contact-gradient current density	mA / m^2
J_{SC}	Short-circuit current density	mA / cm^2
c_0	Global device-current calibration coefficient	Dimensionless
c_1	Linear residual-correction coefficient	Dimensionless
c_2	Quadratic residual-correction coefficient	Dimensionless
λ	Ridge regularization weight	Dimensionless
V_{OC}	Open-circuit voltage	V
FF	Fill factor	% or fraction
η	Power-conversion efficiency	%
R_K	Interfacial charge-transport resistance (EIS middle semicircle)	Ω

1. INTRODUCTION

The mechanism that transforms light into electricity in a dye-sensitized solar cell (DSSC) has four components: a molecule called sensitizer, a mesoporous semiconductor, an electrolyte and a counter electrode [1, 2]. This architecture clearly depends on the nanocrystalline TiO_2 photoanode as it offers a high internal surface area to anchor dye molecules and a percolating path for the injected electrons. Thus, the thickness of the film is not a purely geometric variable. The thicker the layer the higher the dye loading and the higher the optical absorption, but the thicker the layer, the larger the area of the interfaces between the layers where recombination can occur [3, 7-10, 16-18, 25-27].

The two dimensionless combinations are used in most of this competition. The number of attenuations is related to the quantity alpha d for Beer-Lambert type of representation and to the quantity d/L for the film thickness in comparison to the effective electron diffusion length. If the charge collection efficiency is high, but the value of α_d is too low, the light cannot be harvested fully. However, for the d greater than the relevant transport length, the increase in photogeneration is offset by increasing recombination, trapping, electrolyte-transport limitations and ohmic losses. Therefore, there is a possibility of obtaining a maximum in photocurrent or in power conversion efficiency physically, but without a simple monotonic relationship with thickness [16-18, 23-29].

Tsai et al. were able to compress TiO_2 nanoparticle photoanodes that range from 12.7 to 55.2 μm thick [3]. Their experiment is important for physics-based modelling since the thickness was the only variable changed while the fabrication conditions were kept constant. The efficiency at 12.7 μm is 5.43% and at 26.6 μm is 9.01% and decreases with thickness. The film with thickness of 26.6 μm showed the highest J_{SC} and the lowest R_K (charge-transport resistance). The authors suggested that this behavior is due to the competition between two gains (more light is harvested in the dye) and two losses (long electron transport path) [3].

A conventional polynomial or spline can approximate a thickness trend but cannot impose the electron continuity equation. A deterministic PDE, on the other hand, can be used to model transport, but may require effective coefficients that are not seen in all of the specimens. Physics-informed neural networks (PINNs) enforce differential equations and boundary conditions in a neural approximation [4, 5]. For steady linear problems, physics-inspired extreme learning or random-features variants enable to obtain a neural

representation with a reduced cost of back-propagation, which can be solved with a smaller constrained least-squares problem [6, 30]. While these types of models are good for small data sets, physics constraints cannot replace the need for real validation. Nonetheless, the data can be interpolated by the flexible PINN, even if measurements are sparse, and apparent agreement at the training points is not necessarily indicative of predictive generalization [11].

The prior print of the present model was more relaxed inverse neural systems and were very close to training the fit. Although this was a good result for proving feasibility, it was not stringent enough be published as it failed to demonstrate out-of-sample performance and tried to find multiple correlated physical parameters from six devices. Considering the above the present study thus embraces a rather more conservative final model. It sets underdetermined transport constants to specified effective values, validates the neural field against an analytical solution, confines the correction by data to a low order regularized function and processes each thickness by leave-one-out.

The aim is to

(i) Build a thickness parametric physics-informed neural solution of the one-dimensional electron continuity equation.
(ii) Couple the PDE-based collection current with sparsely available device information with minimal regularization.
(iii) Quantify the predictive error by leave one thickness out cross validation.
(iv) Compare the physics-informed neural solution with conventional ANN, polynomial, spline and Gaussian-process baselines.
(v) Conduct physics/data ablation and sensitivity analyses of the framework
(vi) Quantify uncertainty in the predicted optimum thickness, and
(vii) Test the 'frozen' model on an independent published thickness series. The goal of the proposed contribution is not to predict a universal DSSC, but rather the reproducible demonstration of the gain that can be achieved by the physics of transport in a small data thickness modeling, and the rendering of uncertainty and domain shift visible.

2. EXPERIMENTAL DATA, SOURCE CONDITIONS and PREPROCESSING

2.1 Primary Source Dataset

The data of the calibration dataset was copied from Table 1 in Tsai et al. [3]. It is noteworthy that the nanoparticles used to form the TiO_2 paste was the Degussa P25 (25-30 nm), doctor-bladed on FTO glass and compressed mechanically at 420 kg/cm^2 and heat treated at 150 ^{0}C for 90 min and 500 ^{0}C for 30 min. The photoanodes were sensitized by keeping them in the N3 dye solution (0.3 mM) for 5 h. The devices were based on a Pt counter electrode and an iodide/triiodide electrolyte and operated under AM 1.5G illumination at 100 mW/cm^2. Film thickness was measured using the cross-sectional FESEM images and R_K was related to the middle semicircle of the EIS response [3].

Table 1. Source dataset used for PINN training and algebraic efficiency check

Sample	d (μm)	Charge Transport Resistance (R_K) (Ω)	Open Circuit Voltage (V_{OC}) (V)	Short Circuit Current (J_{SC}) (mA / cm^2)	Fill Factor (FF) (%)	Reported η (%)	Recalculated η (%)
A	12.7	19.20	0.71	12.62	60.89	5.43	5.456
B	14.2	12.50	0.68	19.88	57.90	7.80	7.827
C	25.0	10.60	0.68	21.59	58.33	8.59	8.564
D	26.6	9.41	0.68	22.41	59.66	9.01	9.091
E	35.3	9.87	0.66	22.32	56.10	8.30	8.264
F	55.2	10.10	0.62	19.37	54.67	5.85	6.566

All the samples from A to E have this identity, to within 0.1. For sample F, the printed values 0.62 V, 19.37 mA /cm^2, and 54.67% imply 6.566%, whereas the source table reports 5.85%. Both values remained unchanged. The algebraically consistent efficiency was used for training the model, as algebraically inconsistent printed quantities cannot be reproduced in a hard PV identity. This discrepancy is not corrected quietly, rather the source-data uncertainty is recognized.

2.2 Preprocessing and Independent Test Data

The differential equation was modified to use thickness in meters, and the thickness was normalized as z = 2(d-d_{min})/(d_{max} - d_{min})-1, where d_{min} = 12.7 µm and d_{max} = 55.2µm. The spatial coordinate was normalized as x_i = x/d, to ensure that each film is in the same computational domain, with 0 <= x_i <= 1. No experimental values were imputed. Uncertainty was estimated using leave-one-out and jackknife procedures for the Tsai thickness series, since no information was provided about the variance of the measurements.

To test the external transportability, the model was frozen, and then it was applied to the thickness series of Sedghi and Miankushki [12] without a reassessment. They tape-cast and treated their TiO_2 electrodes with $TiCl_4$, sensitized with N719 and filled with iodine electrolyte. The 10.3, 13.1, 15.2 and 21.3 µm thicknesses reported in table 2 of that study had a maximum reported efficiency of 7.5% at 15.2 µm. However, as a result of the different fabrication route, dye concentration, sensitization time, FTO properties and device chemistry, this data set is intended as a challenging domain-shift test and is not intended to mimic the Tsai system.

3. MATHEMATICAL MODEL OF THICKNESS-DEPENDENT ELECTRON TRANSPORT

3.1 Continuity Equation and Normalized Domain

The TiO_2 photoanode was modeled as a one-dimensional homogenous medium from the collecting contact (FTO/TiO_2) at x = 0 to the TiO_2/electrolyte interface at x = d. It is assumed the illumination is steady, the diffusive transport is effective, the recombination is of the first order, the optical attenuation is exponential, the effective transport coefficients are spatially uniform and the six compressed films are in the same state. The trapping of particles at the scale of the particle, the energetic disorder, the diffusion of the electrolyte and the transport depending on the voltage are incorporated in the effective parameters or in the auxiliary outputs.

$$D_e \frac{\partial^2 n_e}{\partial x^2} - \frac{n_e - n_e^0}{\tau} + \varphi\, \alpha\, e^{(-\alpha x)} = 0 \qquad 0 < x < d \quad (1)$$

where n_e is the number of excess electrons at the coordinate x,

n_{e0} is the electron concentration in darkness,
τ is the lifetime of electrons,
φ is the intensity of the light flux,
α is the coefficient of the light absorption,
D_e is the coefficient of electron diffusion,
L is the diffusion length = $\sqrt{D_e\, \tau}$ (2)

3.2 Boundary Conditions and Non-Dimensionalization

Ideal extraction at the FTO contact was considered to be $n_{e0}(0, d) = n_e^0$ at short circuit. Zero normal-flux was assumed at the outer boundary of the photoanode $\left(\frac{\partial n_e}{\partial x}\right)_{x=d} = 0$. The second condition is no electron collection across the electrolyte-side boundary, and does not include the counter electrode within the modeled TiO_2 domain.

$$u\,(\xi, d) = \frac{[n_e\,(x, d) - n_{e0}]}{\varphi\, \alpha\, \tau}, \quad \xi = \frac{x}{d} \qquad (2)$$

The variable physical domains are transformed into one fixed domain by using $\frac{\partial}{\partial x} = \left(\frac{1}{d}\right) \frac{\partial}{\partial x_i}$, and provides

$$\left(\frac{D_e}{d^2}\right)\left(\frac{\partial^2 u}{\partial \xi^2}\right) - u + \exp(-\alpha\ d\,\xi) = 0\,,\quad 0 < \xi < 1 \qquad (3)$$

$$u\,(0,d) = 0,\quad \left(\frac{\partial u}{\partial \xi}\right)_{\xi=1} = 0 \qquad (4)$$

The thickness is explicitly included in equation (3) as $(L/d)^2$ and α_d. Hence, it connects a fabrication parameter which is directly measured in the source experiment with transport and optical attenuation without the need for an empirical thickness factor within the PDE [23-29].

The reason thickness is a physically direct model variable is indicated in equation (4). The ratio L/d determines the balance between the diffusion and recombination rate and α_d determines the optical attenuation. Even if Coefficient of electron diffusion (De), lifetime of electrons (τ) and coefficient of the light absorption (α) are common to all samples both change.

3.3 Contact Current and Device-level correction

The dimensionless neural field provides the gradient of the collection at x_i=0. The nominal transport current is

$$J_{PDE}\,(d) = \frac{q\,D_e\,\varphi\,\alpha\,\tau}{d}\quad \left(\frac{\partial u}{\partial \xi}\right)_{\xi=0} \qquad (5)$$

Variations of dye loading, pore accessibility, packing density, compression uniformity, surface trap density and interfacial kinetics are not all taken into account by a one-dimensional model with shared coefficient. Instead of having their own free parameter for each unmeasured mechanism, a regularized multiplicative residual correction was employed:

$$J_{SC}\,(d) = J_{PDE}\,(d)\exp(c_0 + c_1\,z + c_2\,z^2) \quad (6)$$

c_1 and c_2 were subjected to the L_2 ridge term with λ=0.10, while c_0 is a device current calibration parameter for the whole system. The correction is purposely made at the lower order. It is not able to produce arbitrary oscillations and serve only to absorb any systematic thickness dependent effects that are not included in Eq. (3). First order ridge functions of normalized thickness were used to represent open-circuit voltage and fill factor. This was selected following preliminary capacity checks as it was found to cause more instability but with no consistent reduction in leave-one-out error. No regression of efficiency was done. It was imposed under illumination 100 mW /cm^2.

$$\eta = V_{oc}\,J_{sc}\,FF \quad (7)$$

R_K was not used as a predictive output, but instead as an experimental diagnostic [19-22]. Having only 6 points, the resistance drop from sample A to sample B is quite steep, and the minimum near sample D is very shallow, and may be interpolated nearly exactly by a flexible network, which contains parameters that do not contribute to Eq. (7).

4. PHYSICS-INFORMED NEURAL NETWORK METHODOLOGY

4.1 Random-feature PINN field

The neural state $u_\theta(x_i, d)$ was realized as a single-hidden-layer tanh random-feature network using the general idea of extreme-learning from physics-informed stationary PDEs [6,30]. The input variables are the normalized depth x_i and the normalized thickness z. The number of hidden features generated was 80, once with seed 42. Their weights and biases were then frozen, and the output coefficients optimized. The state was specified as $u=x_i$ softplus(s_θ) to make sure u(0, d) is exactly zero and the excess density remains non-negative. Analytical expressions of the first and second derivatives were used, and therefore, the implementation does not need automatic differentiation software, but instead NumPy and SciPy.

The physics field was trained in a parametric domain of thickness 10-60 μm and $0 <= x_i <= 1$ with 21 thickness collocation levels and 60 spatial points per thickness collocation level. The objective contained the mean-square residual of Eq. (3) and a weighted outer-boundary derivative residual. In the final model, the boundary weight was 50. The effective constants were fixed at D_e=1 x10^{-8} m^2/ s, τ =0.05 s, α =7 x 10^4 m^{-1}, and φ = 4 x 10^{21} photons per (m^2 s), corresponding to L=22.36 μm. These values are not measurements derived from the model, but are

model constants. Repairing them makes it possible to avoid the non-identifiability problem, where several combinations of D_e, τ, α and φ can regenerate six currents.

4.2 Training, Regularization and Reproducibility

The coefficients for the PDE were optimized using trust-region nonlinear least squares. The device correction was then applied to log $[J_{sc}/J_{PDE}]$ to ensure that the current is always positive. The residual correction was constrained by a ridge penalty $\lambda(c_1^2+c_2^2)$, separate ridge penalties of 0.10 were used for the linear V_{OC} and FF mappings. Efficiency followed exactly the equation (7). The final implementation is deterministic for seed 42, provided as a python 3.13 script.

This two-stage setup allows for physics and device calibration to be separated. No J_{SC}, V_{OC}, FF or efficiency value is used to solve the neural field. Thus, for each cross-validation fold the same PDE field is used. Only the small device-correction and auxiliary coefficients are refitted when a thickness is held out. This will ensure the photovoltaic target is not introduced physically via hidden retraining.

4.3 Validation Protocol and baseline models

The validation was done in 4 layers. First, the neural field was compared with the analytical solution of Eq. (3) at all six source thicknesses, where this equation has a constant-coefficient analytical solution. Second, a leave-one-thickness-out cross-validation (LOOCV) was carried out: all device level coefficients were fitted to the other five devices and then J_{SC}, V_{OC}, FF, and efficiency were predicted at the held-out thickness. Third, the same LOOCV splits were applied for linear regression, quadratic regression, natural cubic splines, Gaussian-process regression and a traditional one hidden-layer ANNs. Finally, the last Tsai-trained model was frozen and used on the Sedghi-Miankushki series without changing its parameters.

To summarize the predictive accuracy, the mean absolute error, the root-mean-square error, the mean absolute percentage error (MAPE) and R^2 were used. MAPE and the fold-level errors reported here are more representative of the data than R^2, which can be negative when the range of responses is small, as in the case of N=6. The continuous optimum was obtained by deleting each one of the source devices in turn, refitting the device-level model, finding the maximum on a dense thickness grid and constructing a jackknife interval based on the t5. This is a time interval that is due to sample sensitivity rather than the measurement noise that was not available in the source paper.

5. RESULTS AND DISCUSSION

5.1 Source Trend and Physical Interpretation

The source data exhibit a well-defined thickness optimum. The results demonstrate that the J_{SC} rose from 12.62 mA/cm^2 at 12.7 μm to 22.41 mA/cm^2 at 26.6 μm, whilst the V_{OC} was down across the full thickness range, starting at 0.71 and ending at 0.62 V. R_K was as low as 19.2 ohm at 12.7 micrometers and a minimum of 9.41 ohm at 26.6 μm, staying at around 10 Ω at larger thicknesses. This is consistent with the better optical/dye utilization and particle-network collection up to an intermediate thickness, followed by increasing transport and recombination penalties [3, 16-22, 25-27].

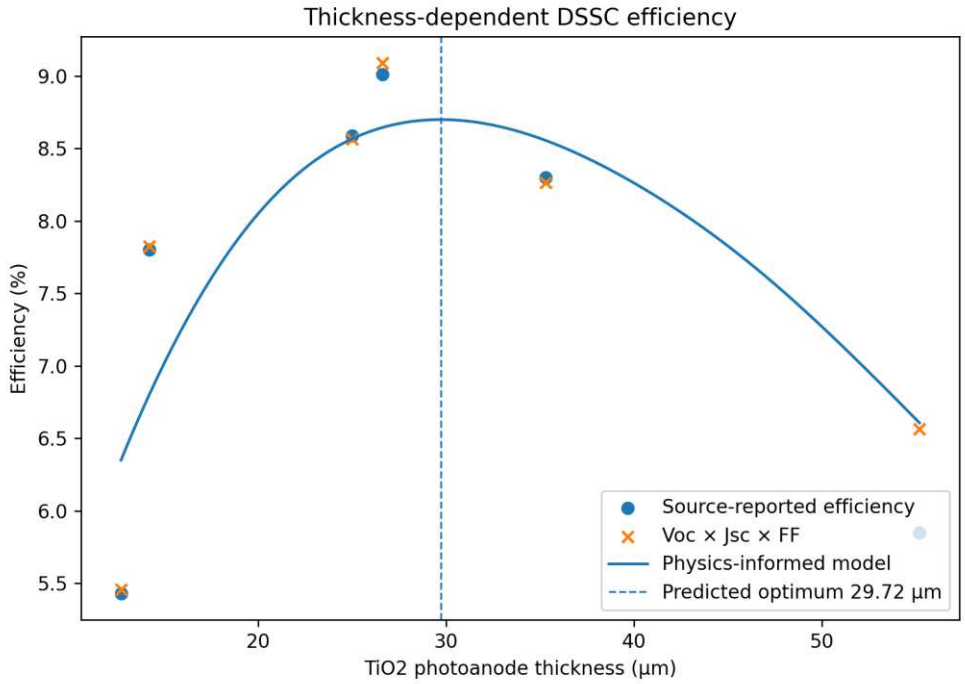


Figure 1. Experimental and modelled efficiency for varying thickness of TiO_2 photoanode. (Efficiencies are shown for source reported and algebraically consistent data as sample F is internally inconsistent)

The regularized continuous model predicted a maximum efficiency of 8.7% at 29.72 µm with J_{SC} = 22.52 mA / cm^2, V_{OC} = 0.669 V and FF = 57.74%. The predicted optimum is higher than the measured 26.6 µm condition, but is still in the high-performance plateau between samples C and E: this was done on purpose as the goal was not interpolation of six samples but predictive robustness.

5.2 Physics-field Verification

Sample	d (µm)	Relative L_2 field error (%)	J_PINN/J_analytical
A	12.7	0.482	0.99748
B	14.2	0.685	0.99673
C	25.0	0.280	1.00129
D	26.6	0.257	1.00114
E	35.3	0.165	0.99921
F	55.2	0.084	0.99961

Table 2. Analytical verification of the physics-informed neural field

The relative L_2 field error at all of the experimental thicknesses was less than 0.7%, with a minimum error of 0.084% and a maximum error of 0.685%. The ratio of PINN contact-gradient current to analytical contact-gradient current was always in the range of 0.99673 to 1.00129. The PDE residual RMSE was $7.65e^{-04}$ and outer-boundary derivative RMSE was $5.17e^{-04}$ throughout the entire collocation domain. As a result, numerical error of the neural PDE solver is much lower than the (device-level) prediction error and the major error source is the error from sparse device calibration and model form instead of from failing to solve Eq. (3).

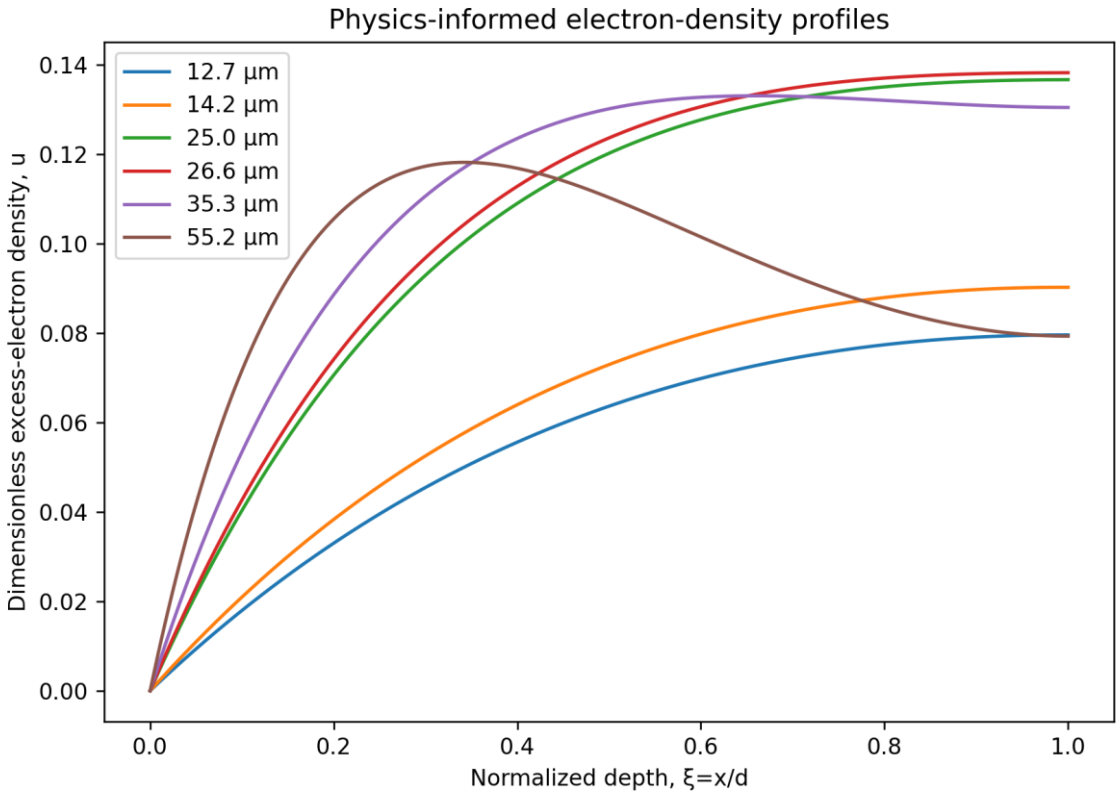


Figure 2. The physics-informed neural field (PINF) predicted the following dimensionless excess-electron-density profiles for the six photoanode thicknesses.

5.3 Training fit after regularization

Table 3. Full data model fit; (η exp* is efficiency re-calculated from printed V_{OC}, J_{SC} and FF)

Sample	Thickness	J_{exp}	J_{model}	V_{exp}	V_{model}	FF_{exp}	FF_{exp}	η_{exp*}	η_{model}
A	12.7	12.62	15.21	0.710	0.699	60.89	59.75	5.456	6.350
B	14.2	19.88	16.40	0.680	0.696	57.90	59.58	7.827	6.800
C	25.0	21.59	21.70	0.680	0.677	58.33	58.30	8.564	8.567
D	26.6	22.41	22.06	0.680	0.674	59.66	58.11	9.091	8.645
E	35.3	22.32	22.74	0.660	0.659	56.10	57.08	8.264	8.556
F	55.2	19.37	19.33	0.620	0.624	54.67	54.73	6.566	6.607

Now, however, the final regularized model does not exhibit the very low training error of the previous high-capacity model. The training MAPE for J_{SC}, V_{OC}, FF, and algebraically consistent efficiency is 7.03%, 1.00%, 1.55%, and 6.44% respectively. This controlled bias is good in a six-device dataset since it does not cause the network to consider every printed value as an exact constraint with no noise. The most significant current residuals are for the two thinnest samples, where there is a large step in Jsc of 12.62 to 19.88 mA cm^2 over a spacing of just 1.5 µm. That step is not captured by a shared smooth transport model unless a very flexible correction is used, indicating that there are unreported properties from film to film that affect the response.

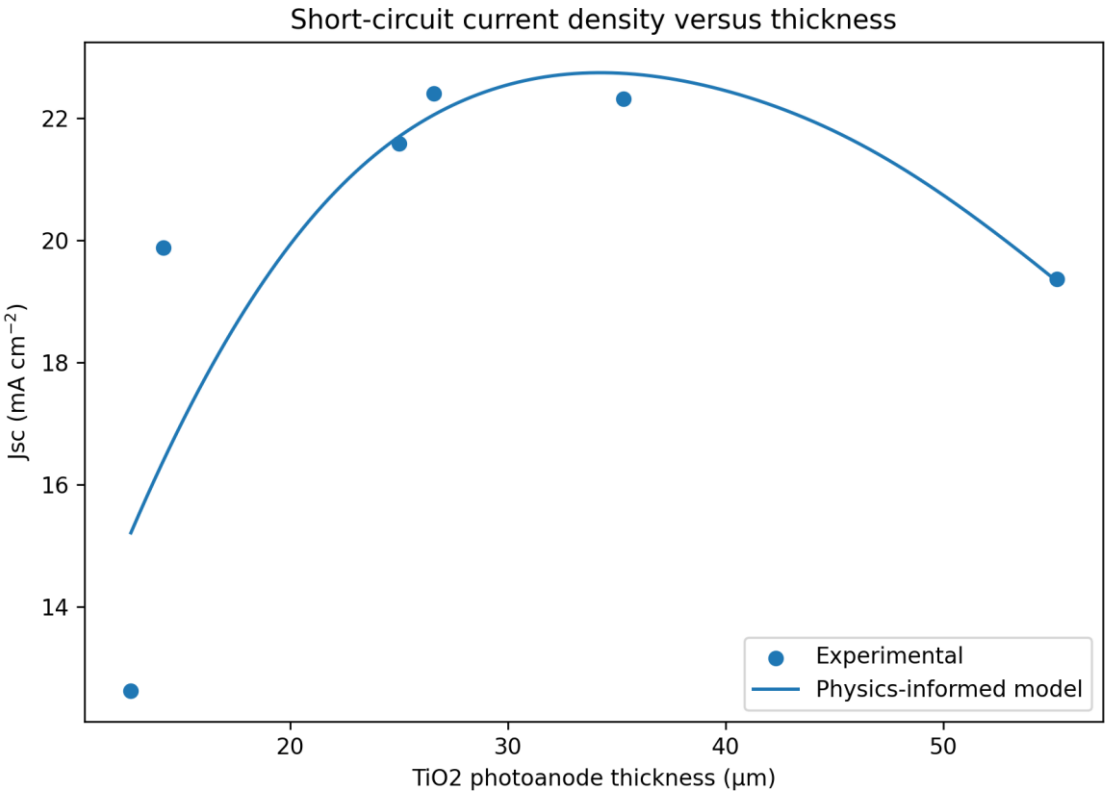


Figure 3. The short-circuit current density predicted by the regularized physics-informed model and measured values of the Tsai thickness series.

5.4 Leave-One-Thickness-Out Predictive Validation

Held out	Thickness	J_{exp}	J_{pred}	V_{exp}	V_{pred}	FF_{exp}	FF_{pred}	η_{exp}	η_{pred}	η_{error} %
A	12.7	12.62	18.71	0.710	0.693	60.89	59.13	5.456	7.660	40.41
B	14.2	19.88	14.38	0.680	0.704	57.90	60.36	7.827	6.109	21.96
C	25.0	21.59	21.74	0.680	0.677	58.33	58.29	8.564	8.576	0.14
D	26.6	22.41	21.91	0.680	0.673	59.66	57.80	9.091	8.524	6.24
E	35.3	22.32	23.05	0.660	0.659	56.10	57.34	8.264	8.711	5.40
F	55.2	19.37	18.74	0.620	0.637	54.67	54.90	6.566	6.551	0.22

Table 4. Leave-one-thickness-out predictions (A model was fitted without each of those whole devices to predict each row)

Across all six folds, LOOCV MAPE was 14.23% for J_{SC}, 1.72% for V_{OC}, 2.16% for FF and 12.40% for efficiency. The interior samples (C-E) had the lowest efficiency errors which were 0.14%, 6.24% and 5.40% respectively. The errors in each of the positions were greatest at A and B where the sharp low thickness current transition was held out at either end point, thus removing the information used to reconstruct that current transition. It is significant that the distinction is made between interpolation and boundary extrapolation. The model can be used to make reasonably informative predictions within the design space measured but cannot extrapolate abrupt film-quality changes away from the adjacent data.

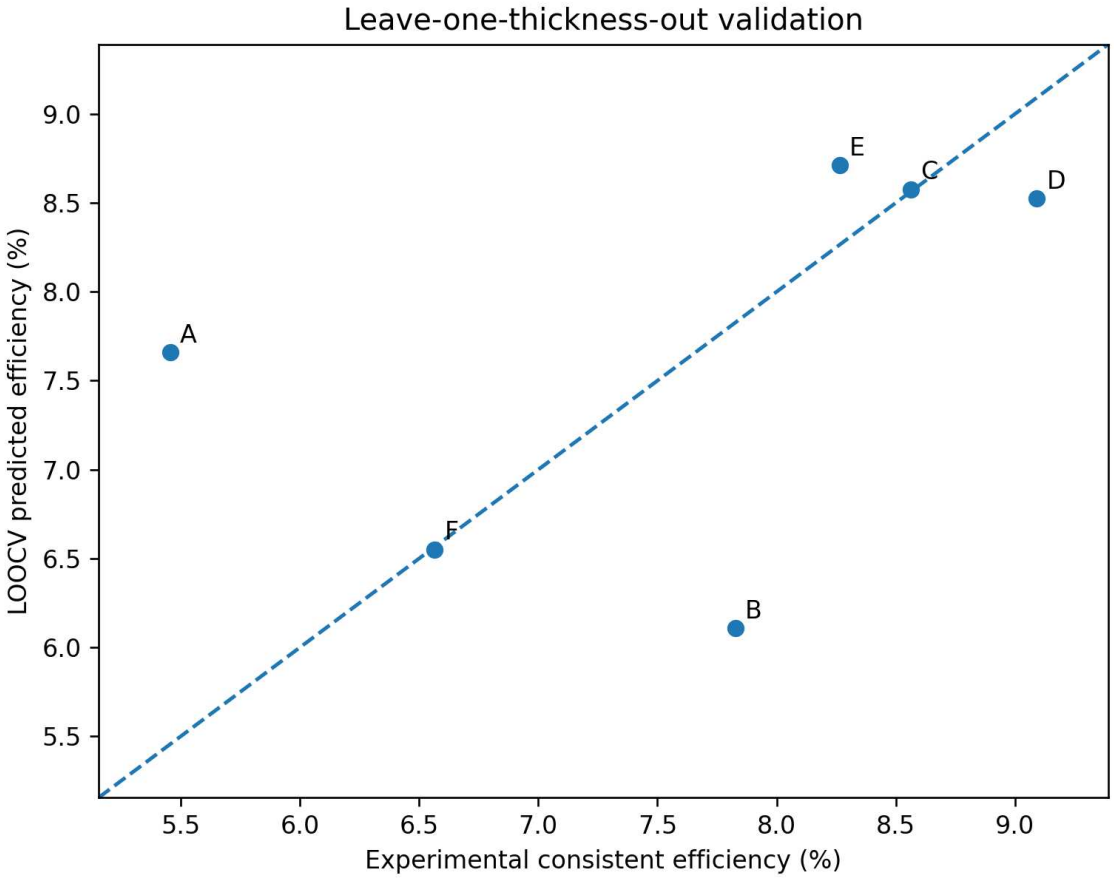


Figure 4. Experimentally and leave-one-thickness-out predicted efficiency (Labels are used to label the missing sample from the source)

5.5 Comparison with Conventional Models

Table 5. Data driven baselines and LOOCV comparison.

Model	J_{SC} MAPE %	V_{OC} MAPE %	FF MAPE %	η MAPE %	η RMSE (pp)
Physics-informed model (final)	14.23	1.72	2.16	12.40	1.179
Linear regression	29.70	1.57	2.15	27.76	2.308
Quadratic regression	26.95	1.53	5.38	26.08	2.321
Natural cubic spline	44.76	3.16	15.13	78.42	9.515
Gaussian process	19.75	3.28	4.04	19.34	1.521
Conventional ANN	19.42	3.84	3.55	20.15	1.681

The physics-informed model had the lowest efficiency MAPE (12.40%) and lowest efficiency RMSE (1.179 percentage points) when compared to the evaluated models. The purely data-driven Gaussian-process regression method achieved the next best performance at 19.34% efficiency MAPE, followed by the conventional ANN with 20.15% efficiency MAPE. For linear regression, the efficiency MAPE was 27.76% while for quadratic regression, the efficiency MAPE was 26.08%. Natural cubic spline interpolation was particularly unstable when extrapolating on the one leave-out boundaries. These results demonstrate the utility of the embedding of the transport shape within a sparse data set and cannot be extended to the present thickness system without outside evidence.

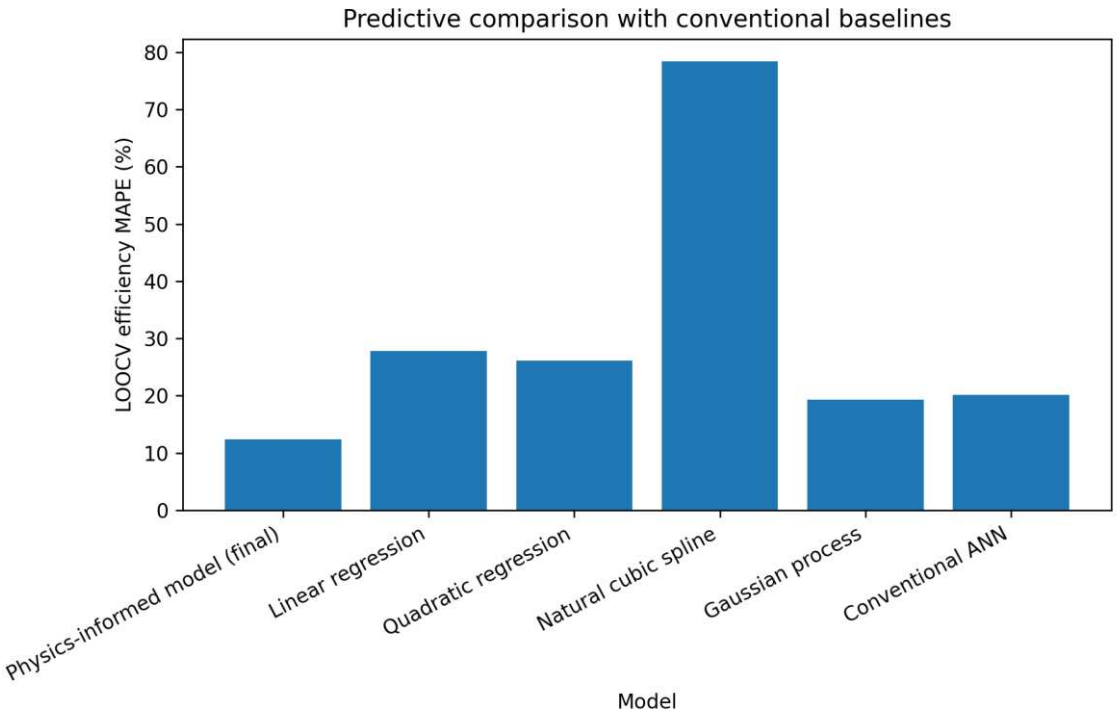


Figure 5. LOOCV efficiency MAPE for physics informed model and conventional data driven baselines.

5.6 Physics/Data Ablation

Table 6. The same leave-one-out folds were used in the physics and data ablation.

Ablation Model	J_{SC} MAPE %	η MAPE %
Nominal physics only (uncalibrated amplitude)	103.50	103.75
Physics + one global current scale	13.85	12.35
Physics + linear residual correction	22.20	20.91
Physics + regularized quadratic correction (final)	14.23	12.40
Data-only conventional ANN	19.42	20.15

The uncalibrated nominal physics model was found to be off by more than 100% because the absolute value of the current amplitude would be dependent on the effective optical and effective carrier-generation quantities which are not readily available from the source table without calibration. Only introducing one global current scale reduced efficiency MAPE to 12.35%, which proved that the PDE already provides most of the useful thickness shape. The final regularized quadratic correction achieved a more faithful full-data representation of the observed non-monotonic current and 12.40% efficiency MAPE, while a linear residual correction impacted validation. The data-only ANN was significantly poorer (20.15%). The small difference between the global-scale and the final hybrid LOOCV errors is also telling: the added quadratic terms are not so much an identification of a unique physical mechanism, as a minor systematic correction.

5.7 Sensitivity and Optimum Uncertainty

Table 7. One-at-a-time physical-parameter sensitivity while the device-level correction and V_{oc}/FF mappings are fixed and the neural PDE field is re-solved for every sensitivity.

Parameter	Multiplier	d_opt (μm)	η_max (%)
D_e	0.8	29.08	8.277
D_e	1.0	29.72	8.700
D_e	1.2	30.27	9.033
τ	0.8	29.08	8.277
τ	1.0	29.72	8.700

τ	1.2	30.27	9.033
α	0.8	30.74	7.886
α	1.0	29.72	8.700
α	1.2	28.87	9.319

During the one-at-a-time physical-parameter sensitivity test, the same 80-feature neural PDE field was re-solved after each perturbation of D_e, τ or α but the learned device-current correction and the V_{OC}/FF mappings were not changed. As a result, exactly the nominal final-model reference: d_{opt} = 29.72 micrometers and η_{max} = 8.700% is the same as the multiplier = 1.0 case.

The physics-informed transport optimum was found to be around 29.08 µm to 30.27 µm with a +/-20% perturbation of D_e or τ and the maximum efficiency was around 8.28% to 9.03%. The effects are the same in this simplified formulation, since D_e τ appears as L_2 in the normalized transport equation. The optical effect of a change in α was more pronounced; a decrease of 20% shifted the optimum towards 30.74 µm and decreased the maximum efficiency to 7.89%, while an increase of 20% shifted it towards 28.87 µm and increased the maximum to 9.32%. The nominal multiplier = 1.0 row is now identical to the final model (29.72 µm, 8.700%). These are not uncertainty distributions of measured material parameters, but are structural sensitivity results.

The PDE boundary term had a small loss-weight sensitivity. When the boundary weight was increased to 100, the mean analytical field error was decreased from 0.413% to 0.259% and the maximum efficiency difference was approximately 0.001 percentage points, with the optimum boundary weight predicted to be in the range 29.67-29.72 µm. The ridge of the residual had a larger but still interpretable effect: λ = 0.05 to 1.0 changed the optimum from 29.84 to 27.76 µm. The obtained value of λ = 0.10 had the lowest LOOCV efficiency MAPE.

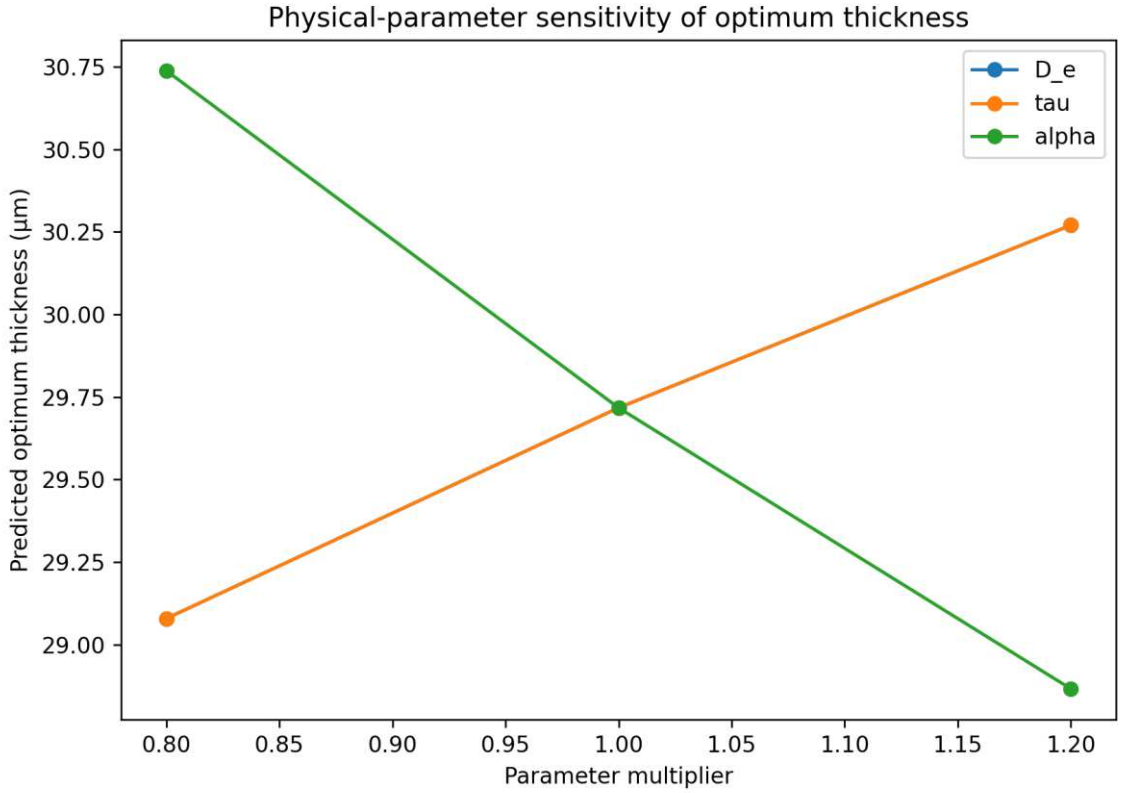


Figure 6. Sensitivity of predicted optimum thickness to variation of ±20% of D_e , τ and α with the calibrated residual correction turned off.

The sampling uncertainty was much larger in the jackknife deletion than in the deterministic sensitivity tests. The six leave-one-out optimum estimates varied between 22.95 to 32.61 µm. Using a T distribution with five degrees of freedom, the approximate 95% jackknife interval for optimum thickness was 12.72-46.72 µm. The corresponding range for maximum efficiency was 8.23 - 9.17%. This is a direct result of the very wide thickness range associated with N=6, and is not a very precisely known fabricating optimum. In future extensions of the present framework, the optimum-thickness uncertainty could be propagated through the governing equation directly using a Bayesian physics-informed neural network formulation and framework instead of post hoc jackknife resampling [14].

5.8 External Transfer to an Independent published Thickness Series

Table 8. This was achieved through strict frozen-model transfer to Sedghi and Miankushki [12] without implementing any recalibration.

Thickness	J_{exp}	J_{frozen}	V_{exp}	V_{frozen}	FF_{exp}	FF_{frozen}	η_{exp}	η_{frozen}
10.3	9.78	13.12	0.646	0.703	78.0	60.0	5.10	5.54
13.1	12.90	15.54	0.641	0.698	71.0	59.7	5.90	6.47
15.2	14.70	17.13	0.660	0.694	77.0	59.5	7.50	7.07
21.3	12.10	20.49	0.631	0.684	76.0	58.7	5.70	8.23

The external test was deliberately rigorous. Efficiency MAPE relative to the externally reported values was 17.10%, the MAPE J_{SC}, V_{OC}, FF were 35.12%, 7.82% and 21.11% respectively. The frozen model underestimated the Sedghi series peak of 15.2 micron which is well below the optimum range of the compressed Tsai system (21.3 µm). This is not a successful universal validation, but is a sign of domain shift. Details of the fabrication method, $TiCl_4$ treatment, N719 sensitization procedure and electrolyte/electrode cannot be simply translated into another system by thickness alone.



Figure 7. The Frozen Tsai trained model has been compared with the independent Sedghi - Miankushki thickness series [12]

Investigating thickness optima by Bandara et al. in an independent study also demonstrates the system dependence of thickness optima [13]. In J_{SC} and efficiency, for their multilayer quasi-solid-state devices, both values increased to the five-layer photoanode and then decreased as the layer number was further increased, while the diffusion length obtained from EIS was not a fixed material constant, but changed with the layer number [13]. When taken together, these external results lend support to the competing light-harvesting, light-transport mechanism, but also demonstrate why the physical thickness-only surrogate is not sufficient.

5.9 Second Independent Transfer Test: an additional published thickness series

To understand if the domain-shift phenomenon observed in Section 5.8 is unique to the Sedghi-Miankushki comparison or is it a general issue with thickness-only transfer, the same model trained on the Sedghi-Miankushki thickness series and frozen was applied, without re-training, to a second independently fabricated thickness series presented by Kumari et al. [15]. The nanocrystalline TiO_2 photoanodes were made by doctor-blading P25 paste without mechanical compression, followed by a 450 ^{0}C for 45 min sintering, and were sensitized with N719 dye (instead of N3) and assembled with a tetrapropylammonium-iodide/I_2/ethylene-carbonate electrolyte. That study's table 1 shows 5 thicknesses ranging from 5.57-20.65 μm with a maximum efficiency of 6.07 ± 0.12% at 12.73 μm, which is less than half of the thickness of the Tsai system. The fabrication-route separation in this system is even greater than the Sedghi-Miankushki comparison due to the differences in compression, sintering protocol, dye and electrolyte used, and a priori would be expected to be at least as challenging a transfer test as the Sedghi-Miankushki comparison.

Table 9. Strict frozen-model transfer, no recalibration was done to Kumari et al. [15]. For consistency with Eq. (7), V_{OC} is converted from the originally reported mV to V.

Thickness d (μm)	J_{exp}	J_{frozen}	V_{exp} (V)	V_{frozen} (V)	FF_{exp} (%)	FF_{frozen} (%)	η_{exp} (%)	η_{frozen} (%)
5.57	10.29	*9.58*	0.730	*0.711*	64.59	*60.60*	4.85	*4.13*
8.64	11.93	*11.65*	0.714	*0.706*	65.48	*60.23*	5.56	*4.95*
12.73	12.98	*15.23*	0.707	*0.699*	65.10	*59.75*	6.07	*6.36*
15.38	12.34	*17.25*	0.706	*0.694*	65.15	*59.44*	5.89	*7.12*
20.65	11.73	*20.22*	0.708	*0.685*	66.64	*58.81*	5.52	*8.14*

The efficiency of the model when applied without any recalibration was 19.78% MAPE relative to the Kumari series (27.76%, 1.97%, and 8.59% MAPEs of J_{SC}, V_{OC} and FF respectively). This efficiency loss is 2.68 percentage points higher than the 17.10% achieved for the Sedghi-Miankushki series, which is in line with the fact that the Kumari and Tsai systems have more fabrication factors (compression state, sintering protocol, dye, and electrolyte) that vary simultaneously. The two thinnest devices (5.57 and 8.64 μm) have been underpredicted by the frozen model, which gives 4.13% and 4.95% efficiencies, respectively, while the experiments show 4.85% and 5.56%. The thicker part of the Kumari series, in contrast, was increasingly overpredicted by it, the most extreme case being at 20.65 μm, when the model predicted 8.14% efficiency but the reported one was 5.52%, and, as mentioned above, the frozen Tsai-trained response continues towards the nominal Tsai-system optimum of 29.72 μm, while the Kumari series is maximum reported at 12.73 μm and drops. In conjunction with Section 5.8, this second independent test also demonstrates that thickness cannot be the only one of the descriptors of a transferable performance surface between the various fabrication routes, and that compression state, sintering history, dye choice, electrolyte composition and transport-related descriptors must be considered as explicit inputs in future extensions to the multivariate approach (Section 6).

6. VALIDATION, ROBUSTNESS AND LIMITATIONS

The validation at the level of the equations is performed well; the neural field matches the analytical constant-coefficient solution with relative L_2 error of less than 1%. Materially, but not as strong, device-level LOOCV is more efficient than the assessed data-driven alternatives. The interior interpolations are significantly more

reliable than the low-thickness boundary prediction. This is again a weaker transfer from outside the system, which supports the model as a within-system physics-regularized surrogate.

The six-point dataset is the main statistical limitation. There are no device replicates and only 6 thickness values, none of which is regularly spaced, which can provide a narrow optimum. Thus, the jackknife interval is quite intentionally given outside the point of optimum. Additional measurements of thickness are particularly needed in the range 14.2-25.0 μm, where there is a significant gap in the main data set and around 25-35 μm where the efficiency maximum is expected. If replicate devices would be available, then the variance of the measurement could be separated from the model uncertainty.

The transport coefficients are not implied, but are effective. It is a methodological shift from the previous inverse with the high capacity and is scientifically better suited for the available data. In Eq. (5), there is strong coupling between D_e, τ, α, φ and the contact gradient. Six steady-state device outputs can be used to infer apparently precise values for all of them, but the values won't be unique. Independent EIS transport times, IMPS/IMVS diffusion information, or wavelength-resolved absorbance, dye loading or transient measurements would be needed to justify parameter-identification claims [19,22,25-29].

Though the device correction of Eq. (6) is very strongly regularized, it is empirical. It is the combination of several real thickness dependent processes, such as: dye loading, light scattering, porosity, particle contact, trap density, electrolyte penetration, and nonideal contact extraction. In the future, this is a residual term that should be substituted with measured explanatory inputs. The thickness-dependent $D_e(d)$, $\tau(d)$ and $\alpha(d)$ can be the outputs of a multivariate model with the inputs being d, porosity, dye loading, surface area, R_K or transport resistance, and experimentally constrained lifetime. This type of formulation would be more transferable to other fabrication systems than a thickness-only calibration [16-22, 25-29].

The simplified one-dimensional steady state equation also neglects nonlinear recombination, the energetic disorder, voltage dependence, series and shunt resistance, ionic transport and finite interfacial extraction. V_{OC} and FF are thus modeled using low-capacity auxiliary functions, and not as direct PDE outputs. Future voltage-dependent transport model should include connections between electron continuity, electrochemical potential and electrolyte kinetics to enable the entire J-V curve to be obtained based on the physical state [7-10, 19-24, 28, 29].

Finally, the source table itself has an efficiency mismatch in Sample F, which is crucial to maintaining the printed/recalculated value in order to maintain reproducibility. The disagreement also shows the reason to not give a model credit just for being able to fit all source numbers. Transparent reporting and sensitivity analysis are more defensible than asking the network to reproduce the same hard physical identity as it was input into the network and hence report an aggregate value.

7. CONCLUSIONS

A conservative thickness-dependent physics-informed neural framework was designed for compressed TiO_2 DSSCs. The normalized diffusion generation-recombination equation contains the thickness of the photoanode explicitly as $(L/d)^2$ and α_d. This parametric PDE was solved by an 80-feature neural field with a sub-0.7% relative L_2 error at all 6 source thicknesses compared to the analytical solution. A low-capacity residual calibration was then used to correlate the PDE contact-gradient current with the current measured at the device, and ridge-linear mappings were used for Voc and FF, and efficiency.

The final model was designed to sacrifice a near-perfect training interpolation for greater validation. The training efficiency (MAPE) was 6.44% and leave-one-thickness-out efficiency (MAPE) was 12.40%. For all of these folds, linear regression, quadratic regression, natural cubic splines, Gaussian-process regression and conventional ANN obtained efficiency MAPEs of 27.76%, 26.08%, 78.42%, 19.34% and 20.15%, respectively. The results of ablation demonstrated that with this physics-based thickness shape and only one global current scale, an efficiency MAPE of 12.35% has been obtained, while a data-only ANN was significantly less capable. The full regularized model predicted a nominal optimum of 29.72 μm and 8.70% efficiency; however the jackknife analysis yielded a very broad interval of thicknesses, indicating that the point optimum is not precisely identified with six devices.

Restricted transfer to an independent published thickness series resulted in an efficiency MAPE of 17.10% and was unable to capture the lower optimal thickness of the external system. This is not a negative outcome but a limitation that in this case, it has been demonstrated that there is not a universal function that defines the

performance of a DSSC as a function of the thickness of the photoanode. A multivariate model with physics constraints, therefore, is the most robust possible extension to the future, for which the measured dye loading, porosity, optical absorption, and transport/recombination quantities derived from the EIS are used. As long as the variables and the range of values remain within the specified limits, the current framework offers a means to combine sparse DSSC information with transport physics which is reproducible and statistically more defensible than either unconstrained interpolation or a high capacity neural fit.

DATA AND CODE AVAILABILITY

The major numerical data have been taken from Table 1 of Tsai et al. [3]. The external transfer data were taken from Table 2 of Sedghi and Miankushki [12] and transcribed. The complete python 3.13 implementation, all prediction and validation tables, sensitivity analyses, figures and the saved neural-field coefficients are provided in the accompanying supplementary package. This study involved no new experimental measurements. The second external transfer dataset (Section 5.9) was transposed from the Table 1 of the paper by Kumari et al. [15].

DECLARATIONS

Ethics approval and consent to participate: Not applicable as this study is based on published aggregate materials data and computational modeling.

Competing interests: This section is to be added by the authors at the time of submission.

Funding: The authors must enter the appropriate funding statement prior to submitting their manuscript.

Author contributions: Author contributions need to be included in the document prior to submitting it using the CRediT taxonomy.

REFERENCES

[1] B. O'Regan, M. Gratzel, A low-cost, high-efficiency solar cell based on dye-sensitized colloidal TiO2 films, Nature 353 (1991) 737-740. https://doi.org/10.1038/353737a0.

[2] M. Gratzel, Photoelectrochemical cells, Nature 414 (2001) 338-344. https://doi.org/10.1038/35104607.

[3] J.K. Tsai, W.D. Hsu, T.C. Wu, T.H. Meen, W.J. Chong, Effect of compressed TiO2 nanoparticle thin film thickness on the performance of dye-sensitized solar cells, Nanoscale Research Letters 8 (2013) 459. https://doi.org/10.1186/1556-276X-8-459.

[4] M. Raissi, P. Perdikaris, G.E. Karniadakis, Physics-informed neural networks: A deep learning framework for solving forward and inverse problems involving nonlinear partial differential equations, Journal of Computational Physics 378 (2019) 686-707. https://doi.org/10.1016/j.jcp.2018.10.045.

[5] G.E. Karniadakis, I.G. Kevrekidis, L. Lu, P. Perdikaris, S. Wang, L. Yang, Physics-informed machine learning, Nature Reviews Physics 3 (2021) 422-440. https://doi.org/10.1038/s42254-021-00314-5.

[6] V. Dwivedi, B. Srinivasan, Physics informed extreme learning machine (PIELM)-A rapid method for the numerical solution of partial differential equations, Neurocomputing 391 (2020) 96-118.

[7] L.M. Peter, Characterization and modeling of dye-sensitized solar cells, Journal of Physical Chemistry C 111 (2007) 6601-6612. https://doi.org/10.1021/jp069058b.

[8] K.D. Benkstein, N. Kopidakis, J. van de Lagemaat, A.J. Frank, Influence of the percolation network geometry on electron transport in dye-sensitized titanium dioxide solar cells, Journal of Physical Chemistry B 107 (2003) 7759-7767. https://doi.org/10.1021/jp022681l.

[9] J. Bisquert, Electron lifetime in dye-sensitized solar cells: Theory and interpretation of measurements, Journal of Physical Chemistry C 113 (2009) 17278-17290. https://doi.org/10.1021/jp9037649.

[10] A. Hagfeldt, G. Boschloo, L. Sun, L. Kloo, H. Pettersson, Dye-sensitized solar cells, Chemical Reviews 110 (2010) 6595-6663. https://doi.org/10.1021/cr900356p.

[11] S. Wang, X. Yu, P. Perdikaris, When and why PINNs fail to train: A neural tangent kernel perspective, Journal of Computational Physics 449 (2022) 110768. https://doi.org/10.1016/j.jcp.2021.110768.

[12] A. Sedghi, H.N. Miankushki, The effect of drying and thickness of TiO2 electrodes on the photovoltaic performance of dye-sensitized solar cells, International Journal of Electrochemical Science 10 (2015) 3354-3362.

[13] T.M.W.J. Bandara, M.A.K.L. Dissanayake, W.J.M.J.S.R. Jayasundara, I. Albinsson, B.-E. Mellander, Efficiency enhancement and chrono-photoelectron generation in dye-sensitized solar cells based on spin-coated TiO2 nanoparticle multilayer photoanodes and a ternary iodide gel polymer electrolyte, Journal of Materials Science: Materials in Electronics 34 (2023) 1969. https://doi.org/10.1007/s10854-023-11252-6.

[14] L. Yang, X. Meng, G.E. Karniadakis, B-PINNs: Bayesian physics-informed neural networks for forward and inverse PDE problems with noisy data, Journal of Computational Physics 425 (2021) 109913. https://doi.org/10.1016/j.jcp.2020.109913.

[15] J.M.K.W. Kumari, N. Sanjeevadharshini, M.A.K.L. Dissanayake, G.K.R. Senadeera, C.A. Thotawatthage, The effect of TiO_2 photo anode film thickness on photovoltaic properties of dye-sensitized solar cells, Ceylon Journal of Science 45(1) (2016) 33-41. https://doi.org/10.4038/cjs.v45i1.7362.

[16] I. Shin, H. Seo, M.-K. Son, J.-K. Kim, K. Prabakar, H.-J. Kim, Analysis of TiO2 thickness effect on characteristic of a dye-sensitized solar cell by using electrochemical impedance spectroscopy, Current Applied Physics 10 (2010) S422-S424. https://doi.org/10.1016/j.cap.2009.12.039.

[17] M.G. Kang, K.S. Ryu, S.H. Chang, N.G. Park, J.S. Hong, K.-J. Kim, Dependence of TiO2 film thickness on photocurrent-voltage characteristics of dye-sensitized solar cells, Bulletin of the Korean Chemical Society 25 (2004) 742-744. https://doi.org/10.5012/bkcs.2004.25.5.742.

[18] M.C. Kao, H.Z. Chen, S.L. Young, C.Y. Kung, C.C. Lin, The effects of the thickness of TiO2 films on the performance of dye-sensitized solar cells, Thin Solid Films 517 (2009) 5096-5099. https://doi.org/10.1016/j.tsf.2009.03.102.

[19] Q. Wang, J.-E. Moser, M. Gratzel, Electrochemical impedance spectroscopic analysis of dye-sensitized solar cells, Journal of Physical Chemistry B 109 (2005) 14945-14953. https://doi.org/10.1021/jp052768h.

[20] L. Han, N. Koide, Y. Chiba, T. Mitate, Modeling of an equivalent circuit for dye-sensitized solar cells, Applied Physics Letters 84 (2004) 2433-2435. https://doi.org/10.1063/1.1690495.

[21] N. Koide, A. Islam, Y. Chiba, L. Han, Improvement of efficiency of dye-sensitized solar cells based on analysis of equivalent circuit, Journal of Photochemistry and Photobiology A: Chemistry 182 (2006) 296-305. https://doi.org/10.1016/j.jphotochem.2006.04.030.

[22] T. Hoshikawa, T. Ikebe, R. Kikuchi, K. Eguchi, Effects of electrolyte in dye-sensitized solar cells and evaluation by impedance spectroscopy, Electrochimica Acta 51 (2006) 5286-5294. https://doi.org/10.1016/j.electacta.2006.01.053.

[23] J. Ferber, R. Stangl, J. Luther, An electrical model of the dye-sensitized solar cell, Solar Energy Materials and Solar Cells 53 (1998) 29-54. https://doi.org/10.1016/S0927-0248(98)00005-1.

[24] S. Sodergren, A. Hagfeldt, J. Olsson, S.-E. Lindquist, Theoretical models for the action spectrum and the current-voltage characteristics of microporous semiconductor films in photoelectrochemical cells, Journal of Physical Chemistry 98 (1994) 5552-5556. https://doi.org/10.1021/j100072a023.

[25] F. Cao, G. Oskam, G.J. Meyer, P.C. Searson, Electron transport in porous nanocrystalline TiO2 photoelectrochemical cells, Journal of Physical Chemistry 100 (1996) 17021-17027. https://doi.org/10.1021/jp9616573.

[26] J. van de Lagemaat, A.J. Frank, Nonthermalized electron transport in dye-sensitized nanocrystalline TiO2 films: transient photocurrent and random-walk modeling studies, Journal of Physical Chemistry B 105 (2001) 11194-11205. https://doi.org/10.1021/jp0118468.

[27] N. Kopidakis, K.D. Benkstein, J. van de Lagemaat, A.J. Frank, Transport-limited recombination of photocarriers in dye-sensitized nanocrystalline TiO2 solar cells, Journal of Physical Chemistry B 107 (2003) 11307-11315. https://doi.org/10.1021/jp0304475.

[28] J.A. Anta, F. Casanueva, G. Oskam, A numerical model for charge transport and recombination in dye-sensitized solar cells, Journal of Physical Chemistry B 110 (2006) 5372-5378. https://doi.org/10.1021/jp056493h.

[29] J. Ferber, J. Luther, Modeling of photovoltage and photocurrent in dye-sensitized titanium dioxide solar cells, Journal of Physical Chemistry B 105 (2001) 4895-4903. https://doi.org/10.1021/jp002928j.

[30] G.-B. Huang, Q.-Y. Zhu, C.-K. Siew, Extreme learning machine: theory and applications, Neurocomputing 70 (2006) 489-501. https://doi.org/10.1016/j.neucom.2005.12.126.